

Global Observations of Upper-Tropospheric Water Vapor Derived from TOVS Radiance Data

GRAEME L. STEPHENS, DARREN L. JACKSON, AND IAN WITTMAYER

Department of Atmospheric Science, Colorado State University, Fort Collins, Colorado

(Manuscript received 8 November 1994, in final form 12 July 1995)

ABSTRACT

This paper describes a physically based method for the retrieval of upper-tropospheric humidity (UTH) and upper-tropospheric column water vapor (UTCWV) based on the use of radiance data collected by the TIROS Operational Vertical Sounder (TOVS), principally channels 4 (14.2 μm), 6 (13.7 μm), and 12 (6.7 μm) of High-Resolution Infrared Radiation Sounder. This paper demonstrates how TOVS radiance data, particularly that of the upper-tropospheric water vapor channel 12, can be modeled usefully using a single band Malkmus model with parameters tuned to a particular sensor on a particular satellite. A significant uncertainty arises from the treatment of continuum absorption, even in regions where line absorption is dominant. This uncertainty can introduce a bias as large as 2 K, which in turn leads to an uncertainty of approximately 15%–20% in the retrieved UTH and UTCWV. The research described in this paper points to the critical need for high-accuracy measurements of upper-tropospheric water vapor to test retrievals such as the one described herein. The results suggest that the relative humidity of the upper troposphere, especially over the domain of the Hadley circulation taken to be between 30°N and 30°S, undergoes a significant seasonal change. This is contrary to the usual assumption of fixed relative humidity adopted in simple climate feedback studies. Large seasonal changes in the region from 30°N to 30°S are possibly associated with the seasonal swings in the Hadley circulation. Similar seasonal changes in the 350-hPa overburden indicate that these swings in relative humidity occur as a result of significant seasonal shifts in the upper-tropospheric water vapor content. In the region equatorward of 30° latitude, the Southern Hemisphere winter is shown to be significantly drier than the Northern Hemisphere winter. This enhanced drying is consistent with the existence of more extensive regions of subsidence producing larger regions of dry upper-tropospheric air in the SH during winter than in the corresponding NH during winter, especially in the subtropical Eastern Hemisphere. Analyses of the data show the clear effects of moistening in the NH subtropics through the monsoonal circulations over Asia and North America and little effect of monsoon circulation in the Southern Hemisphere.

1. Introduction

Water vapor is an essential constituent of the earth's climate system. It plays a decisive role in the radiative transfer within and from the atmosphere and is germane to the transport and release of latent heat in the atmosphere and the rate of evaporation at the surface. The transport of water vapor also fundamentally controls where and why clouds form and thus is crucial to understanding the role of clouds in climate.

The precise way in which water vapor acts as a greenhouse gas is now being tested using global satellite data. For instance, recent studies examine the basic relationships between the amount of water vapor in the atmosphere and components of the earth's climate

system, such as temperature (Stephens 1990) and the earth's radiation budget (Stephens and Greenwald 1991; Bony and Duvel 1994; Webb et al. 1994; Stephens et al. 1994), in an attempt to clarify its role as a greenhouse gas. Despite these studies, the feedback between water vapor, radiation, and global temperature, considered so fundamental to our climate system, has come under critical review by Lindzen (1990), who argues that a global warming will lead to a general drying of the upper troposphere due to enhanced subsidence accompanying any supposed increase in convection. Since an upper-tropospheric drying leads to an increase in the emission to space, the proposed positive feedback between water vapor, temperature, and emission is weakened or, as Lindzen proposed, reversed, implying that global warming may actually be overestimated in present models. Pierrehumbert (1994) argues that the drying associated with large-scale subsidence plays a fundamental role in keeping the water vapor feedback in check. Although the suggestion that the upper troposphere on the whole dries under the scenario of a global warming has been criticized (Betts

Corresponding author address: Prof. Graeme L. Stephens, Dept. of Atmospheric Science, Colorado State University, Fort Collins, CO 80523.

E-mail: stephens@langley.atmos.colostate.edu

1990; Rind et al. 1991), it is a reminder of the pronounced sensitivity of the outgoing emission of infrared radiation to both the amount and distribution of upper-tropospheric water vapor.

Despite the prominent role of water vapor in defining the earth's climate, relatively little effort has gone into analyses of existing global observations, and only modest resources have been spent on developing new technologies to accommodate observational needs. The task of simply determining the global distributions of water vapor above 500 hPa, let alone understanding its possible role in climate and global change, remains elusive. Conventional sonde measurements of upper-tropospheric moisture are unreliable (Elliott and Gaffen 1991), and the quality of any relationship between satellite radiometric data and upper-tropospheric water vapor, like those described in this paper, remains uncertain largely due to a severe lack of verification data. Nevertheless, the fundamental importance of water vapor to climate dictates that these satellite data be analyzed, if for no other reason than to provide motivation for validation.

The principal objective of the research described in this paper is to introduce a method for the retrieval of upper-tropospheric humidity (UTH) and upper-tropospheric column water vapor (UTCWV) based on the use of radiance data collected by the TIROS Operational Vertical Sounder (TOVS). This research expands upon similar research that uses measurements in the $6.3\text{-}\mu\text{m}$ water vapor band by sensors on geostationary satellites (Schmetz and van de Berg 1994; van de Berg et al. 1991; Soden and Bretherton 1993), on polar orbiting satellites (e.g., Raschke and Bandeen 1967; Hayden et al. 1981), and on previous research using TOVS (Wu et al. 1993). The satellite data employed in this study are derived from the HIRS and their characteristics are reviewed in section 2 followed by a discussion of atmospheric profile data in section 3. A model of the infrared radiative transfer is introduced in section 4, and a discussion of transmission models for bands corresponding to selected TOVS channels is given. A theoretical basis for the retrieval schemes introduced in this paper is contained in section 5. Section 6 introduces the retrieval approach for UTH and presents results of this retrieval. Section 7 describes the retrieval of UTCWV and presents results of this retrieval.

2. Satellite radiance data

Detailed characteristics of the data used in this study are described by Wu et al. (1993) and further by Bates et al. (1996). The data used in this study are for the period from January 1989 to December 1991 and are obtained from the operational processing of TOVS by the National Environmental Satellite Data and Information Service (NESDIS). The TOVS package con-

sists of three separate sounding units: the Microwave Sounding Unit (MSU), the Stratospheric Sounding Unit (SSU), and the High Resolution Infrared Radiation Sounder (HIRS). The HIRS data obtained from three IR channels, identified as channels 4, 6, and 12 and centered approximately at 704 , 732 , and 1484 cm^{-1} , respectively, provide the primary source of information used in this study. Channels 4 and 6 are located in the $15\text{-}\mu\text{m}$ CO_2 band and are used for operational temperature sounding, whereas channel 12 is located within the $6.3\text{-}\mu\text{m}$ vibrational-rotational band of water vapor and is sensitive to changes in upper-tropospheric moisture and temperature. All radiances used in this study have been limb corrected by the op-

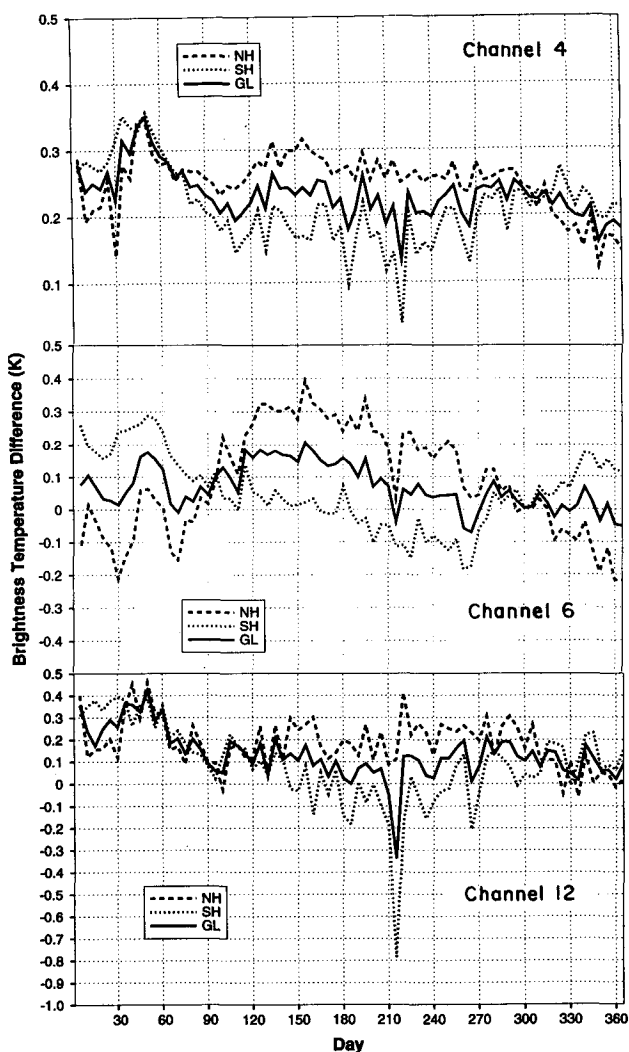


FIG. 1. NOAA-10 minus NOAA-11 differences in A.M. and P.M. averages of channel 4, 6, and 12 N_* brightness temperatures as a function of the 1989 day count. Averages over the Northern Hemisphere, Southern Hemisphere, and globe are labeled as NH, SH, and G*. Temperature averages are weighted by area.

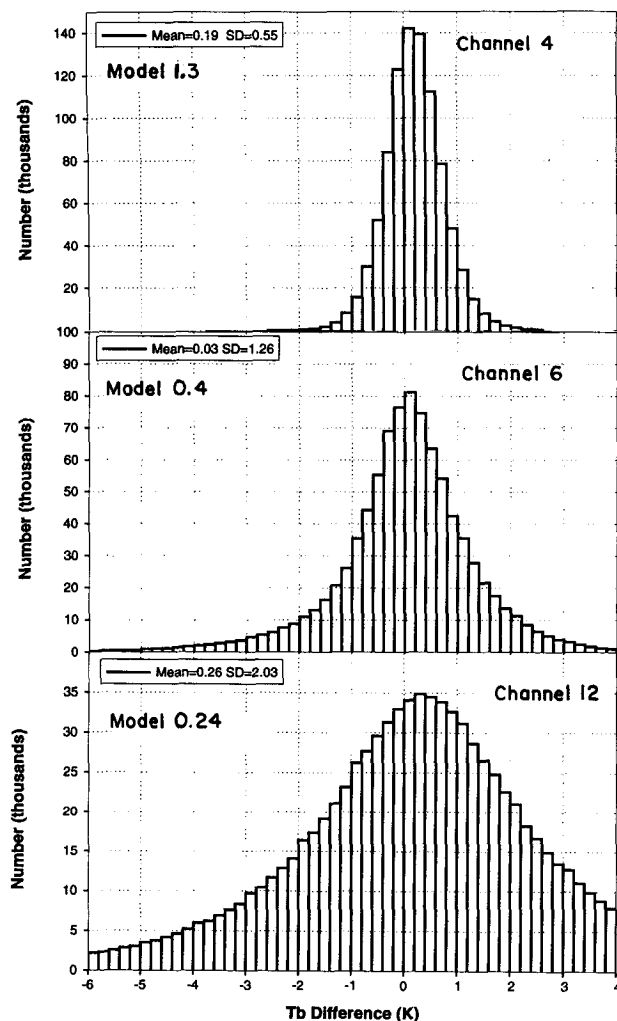


FIG. 2. Histograms NOAA-10 minus NOAA-11 temperature difference annual and global data, given on these diagrams as the mean differences, the standard deviations, and modeled differences in brightness temperature.

erational NESDIS TOVS processing package (Werbowski 1981; see also Kidwell 1991 for documentation of the TOVS channel characteristics, data products, and formats).

A significant effort has been spent at NESDIS to establish a clear-sky radiance data subset of TOVS (e.g., Smith et al. 1979; and further upgraded by McMillin and Dean 1982; and Swaroop et al. 1988). These clear-sky radiances, referred to as N_* radiances, are used in this study. The clear-sky radiances using N_* 's as compared to an alternative approach discussed in Wu et al. (1993) differ by less than 2 K for channel 12. Although this difference is relatively small, the issue of cloud clearing or masking satellite data is currently a topic of much research, especially as we build

toward the launch of the Earth Observatory Satellite (EOS) platforms. Possible cloud contamination of the radiance data used in this study is a major concern that will be addressed in further studies. Wu et al. (1993) also provide an extensive error analysis of channel 12 and show that the angular correction scheme used operationally by NESDIS as well as errors resulting from a combination of instrument factors leads to a total error of approximately 2.5 K.

a. Intersatellite brightness temperature differences

Potentially more problematic are the differences that exist between measurements obtained from different versions of HIRS instruments on different satellites. The results of the present study are restricted to measurements obtained from sensors flown on both the NOAA-10 and NOAA-11 satellites. While further discussion of this issue is warranted, it is only briefly addressed here since it is dealt with more extensively by Bates et al. Examples of the intersatellite differences are shown in Fig. 1 in the form of globally and hemispheric averaged channel 4, 6, and 12 N_* area-weighted brightness temperatures (hereafter referred to as T4, T6, and T12, respectively). These area-weighted data are presented as 5-day means (hereafter referred to as pentad means). Pentad means of the A.M. and P.M. orbits of both NOAA-10 and NOAA-11 satellites are differenced and plotted as a function of time in Fig. 1.

The brightness temperature difference data shown are also depicted in the form of histograms in Figs. 2a–c. The mean NOAA-10 minus NOAA-11 brightness temperature differences (in this case not weighted by area) are given on these diagrams as are the standard deviations. These average data are presented so as to compare more directly with model-simulated brightness temperatures derived from individual profile data. Equivalent satellite-to-satellite rms differences in brightness temperature derived from the radiative transfer model applied to the 1761 different atmospheric profiles described below are also given on the diagrams. It will also be mentioned below how these simulations use the published filter functions corresponding to channels 4, 6, and 12 of the HIRS on NOAA-10 and NOAA-11. The simulated differences are generally similar to the actual brightness temperatures, suggesting that differences in the filter functions defining each channel of the instrument on different satellites could explain a significant amount of the observed differences. However, there could be a variety of other possible reasons for the biases shown. For all results presented below, we apply a simple adjustment procedure by using NOAA-10 as a baseline and subtracting the mean observed biases deduced from the NOAA-11 brightness temperatures shown in Fig. 2.

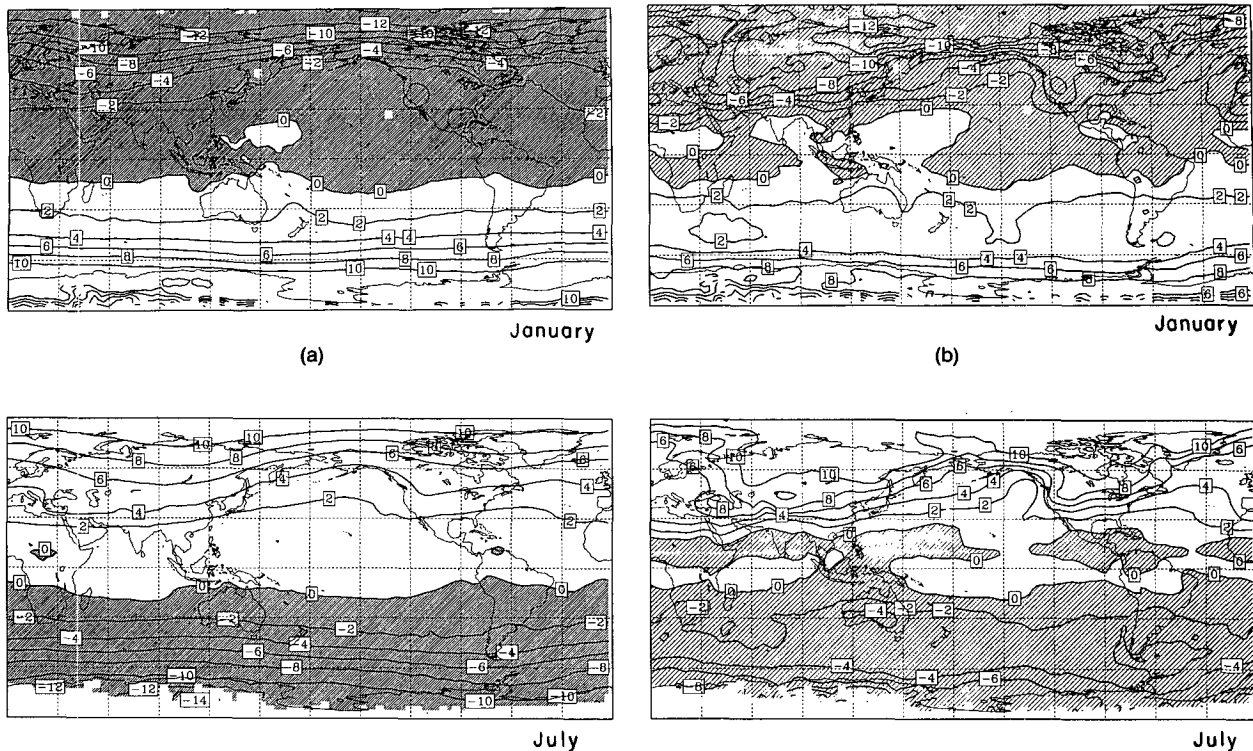


FIG. 3. January and July 1989 monthly mean composites of the (a) T4, (b) T6, and (c) T12 minus the respective annual mean temperatures.

b. Brightness temperature composites

Maps of the A.M. and P.M. pixel radiances using data composited from *NOAA-10* and *NOAA-11* satellites were produced by binning data and averaging to create global and monthly mean distributions of radiances and products derived from pixel-level radiances. Examples of the January and July 1989 monthly mean composites of the T4, T6, and T12, minus the respective annual mean temperatures, are shown in Figs. 3a–c. A clearer, more physical interpretation of these temperatures follows from the consideration of the weighting functions discussed below. For the purpose of interpretation, however, it is relevant to note that the cited levels of maximum contributions of channels 4, 6, and 12 are 280 hPa, 725 hPa, and 400 hPa, respectively (Smith et al. 1979), although a single value of the latter is meaningless. Further discussion of how different layers of the atmosphere contribute to channel 12 radiances is given below.

One of the main features of the distributions shown in Fig. 3a, and to a lesser extent in Fig. 3b, is the relatively small variability of brightness temperature in the Tropics. The relatively uniform temperature across the Tropics is a known characteristic of the tropical atmosphere (e.g., Peixoto and Oort 1992). By contrast, T12 possesses significant variability in these regions in a manner associated with large-scale organization of

deep convection in the intertropical convergence zones and subsidence poleward of these convective areas. Since Figs. 3a and 3b suggest that variations of the thermodynamic temperature across these regions are small, it is reasonable to suggest that the brightness temperature variations, evident in Fig. 3c, between approximately 30°S and 30°N arise largely through moisture variations that occur in the upper troposphere. This is substantiated below in discussion of the retrieval of column water vapor amounts.

Figures 4a and 4b present the pentad-mean channel 4, 6, and 12 brightness temperatures averaged between 0°–30°N and S and between 30°S–30°N (Fig. 4a) and averaged between 0°–60°N and S and between 60°S and 60°N (Fig. 4b). The temperatures used to produce these area averages were derived from a composite of *NOAA-10* and *NOAA-11* N_* radiances and averaged over consecutive five-day periods for 1989. The results are shown as a function of day count and reveal seasonal shifts in hemispheric brightness temperature. The smallest amplitude of the annual cycles shown in Fig. 4a corresponds to the upper-tropospheric temperature channel 4. This temperature cycle has a peak-to-peak value of approximately 1.5 K for the 0°–30°N average and a maximum that occurs during the summer season. By contrast, there is little seasonality in the corresponding 0°–30°S averages. Similar features exist in the an-

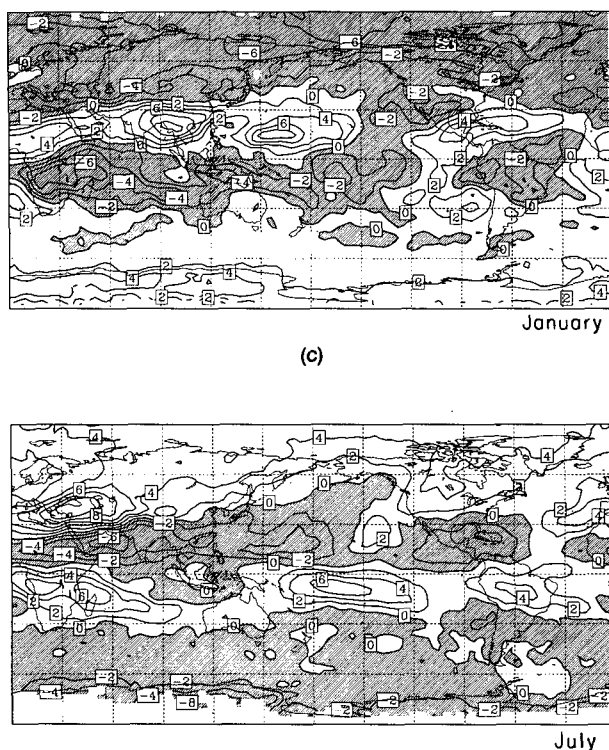


FIG. 3. (Continued)

nual cycles of the channel 6 averaged temperatures, although the 0° – 30° S averages display a slightly more enhanced seasonality that is out of phase with the NH temperatures and is smaller in amplitude (a peak-to-peak amplitude of approximately 1 K). The relatively small amplitudes of the annual cycle in the mid- (T6) and upper- (T4) tropospheric temperatures are also consistent with our understanding of the thermodynamic nature of the tropical atmosphere (e.g., Peixoto and Oort 1992).

Hemispheric averages of channel 12 temperatures reveal a more pronounced annual cycle than the averages of either channel 4 or 6. This is highlighted by marked seasonal shifts defined by a broad maximum occurring between day 180 and 270 in the SH and a corresponding broad minimum in the NH during the same period. It is also relevant to note how the phasing of the cycles of channel 12 hemispheric temperatures opposes that of channels 4 and 6. The peak-to-peak amplitudes of these annual cycles are approximately 4–5 K for the SH and 3 K for the NH, respectively. The principal reason for these larger amplitude features of channel 12 in the Tropics is that the effects shown are largely due to seasonal shifts in upper-tropospheric moisture: with the minimum in the NH corresponding to moistening through tropical convection and the maximum in the SH occurring through the subsidence dry-

ing that is also related to the NH convection. The maximum temperatures during the NH winters are smaller than the SH counterparts, suggesting that distinct interhemispheric asymmetries exist in the convection–subsidence process and the large-scale circulations driven by this process.

The amplitudes of the 0° – 60° N and S annual cycles of channel 4 and 6 temperatures are larger than the 0° – 30° N and S averages due to the larger seasonal swings in atmospheric temperature that occur in the midlatitudes (Fig. 4b). Effects of land heating produce a residual cycle in the channel 6 60° S– 60° N averages that is in phase with the NH cycle. The annual cycles of channel 12 temperatures shown in Fig. 4b for the 0° – 60° N and S regions are even more complex than for tropical regions with both the NH and SH temperatures tracking each other in phase. This highlights the complex nature of both temperature and moisture effects on the spectral emission at the wavelengths of channel 12. In the NH, the summer maximum is most likely due to an increase in upper-tropospheric temperature consistent with the observed increases of channel 4 and 6 temperatures. The SH T12 averages, by contrast, possess a wintertime warming. This result is consistent with the interpretation that the upper troposphere is dryer in the winter hemisphere, as implied in the work of Pierrehumbert and Yang (1993).

3. TIGR2 atmospheric profile data

The forward radiative transfer simulations employ the profile information collected and stored as part of the TIGR2 database (Scott et al. 1991). These profiles are grouped into air mass categories in Table 1. While it is not the intention of this study to provide a detailed characterization of these data, it is nevertheless appropriate to comment on the properties of these profiles for later reference. For this purpose, we adopt the approach of Boers and Prata (1995), who use conservative-variable diagrams as a way of grouping a large body of sounding data into climatological regimes.

The form of conservative variable diagram used in this study is defined with the (liquid water) potential temperature as the vertical coordinate and the total water mixing ratio as the horizontal coordinate. The principle reason for using θ – q_T diagrams is that these thermodynamic parameters are essentially independent of each other with one (θ) closely representing thermal structure and the other (q_T) representing moisture structure.

As Boers and Prata show, θ – q_T diagrams are particularly useful for comparing thermodynamic properties of different climatological regimes. The reason for this is that isentropic displacement conserves θ and q_T , and properties arising from this displacement are easily identifiable on the diagram. As an explanation of this, Fig. 5a is a schematic of an idealized circulation,

which may be thought of as the Hadley circulation, and Fig. 5b is the corresponding $\theta-q_r$ diagram associated with this idealized flow. Air in a well-mixed boundary layer, with thermodynamic properties that largely determined by ocean surface fluxes, is moistened and warmed (Fig. 5b) as it flows to the ITCZ along $D \rightarrow A$ where it ascends moist adiabatically along $A \rightarrow B$ and exits near the tropopause. As this air moves poleward ($B \rightarrow C$), it radiatively cools and subsides ($C \rightarrow D$), conserving its small water vapor content. The cycle is completed as the subsiding air reenters the boundary layer with lower θ and is subsequently warmed and moistened as it flows equatorward.

The conservative diagram analyses was applied to all TIGR2 profiles, and the results of these analyses are presented in Fig. 6 for the tropical and midlatitude air-mass categories given in Table 1. These figures all display the classic triangular shape indicative of thermodynamic constraints on atmospheric profiles. We note that the profiles of these categories contain few cases of deep moist ascent, and they suggest that many of the

TABLE 1. TIGR2 air-mass classifications.

Atmospheric profile number	Air mass
1–322	Tropical
323–710	Midlatitude 1
711–1064	Midlatitude 2
1065–1168	Polar 1
1169–1761	Polar 2

profiles have properties characteristic of the subsidence process ($C \rightarrow D$).

4. Radiative transfer calculations

The retrieval approach developed below is based on results obtained from a numerical radiative transfer model. The model relevant to this study solves the monochromatic transfer equation

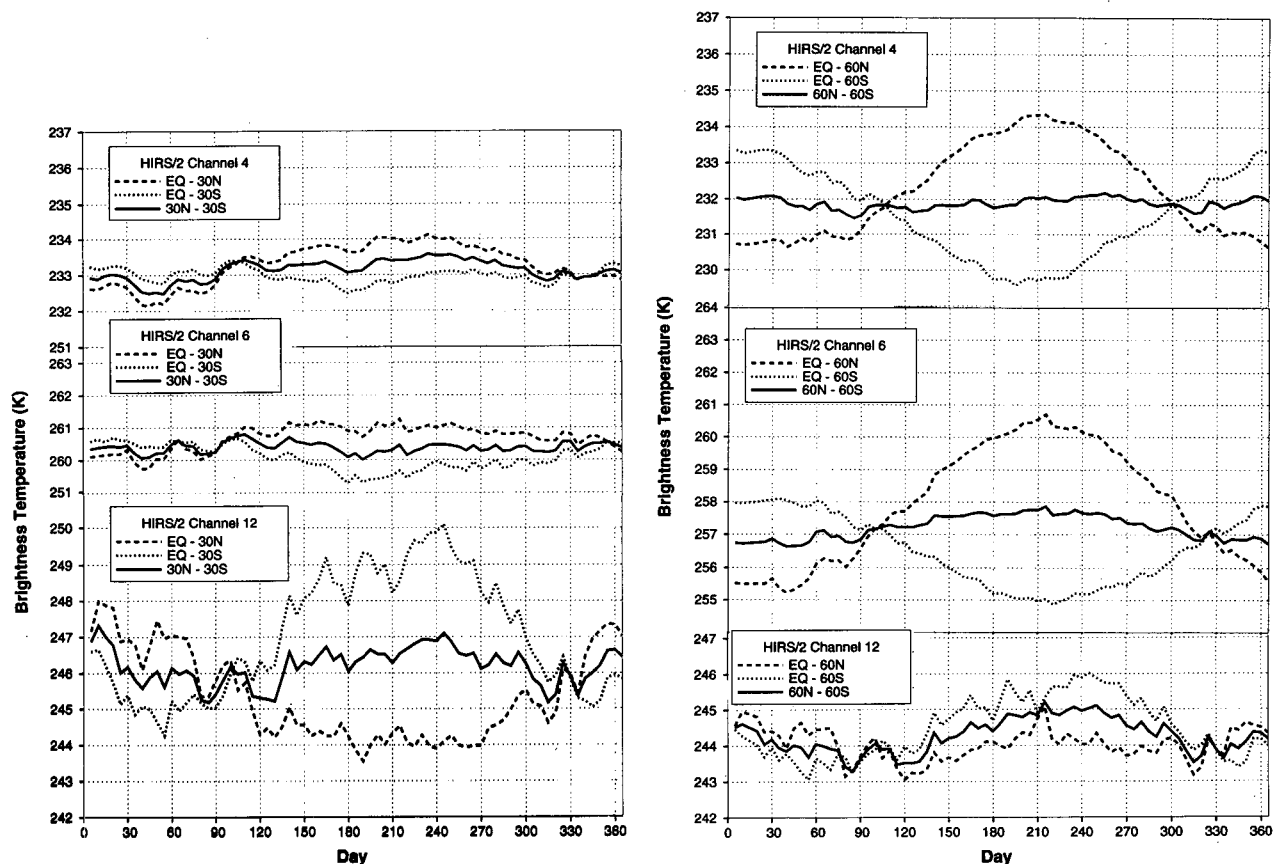


FIG. 4. (a) T4, T5, and T12 averaged between 0° and 30°N and S and between 30°S and 30°N (left) and (b) averaged between 0° and 60°N and S and between 60°S and 60°N (right). The temperatures used to produce these area averages are composites of NOAA-10 and NOAA-11 N_* radiances. They are averaged over consecutive 5-day periods for 1989.

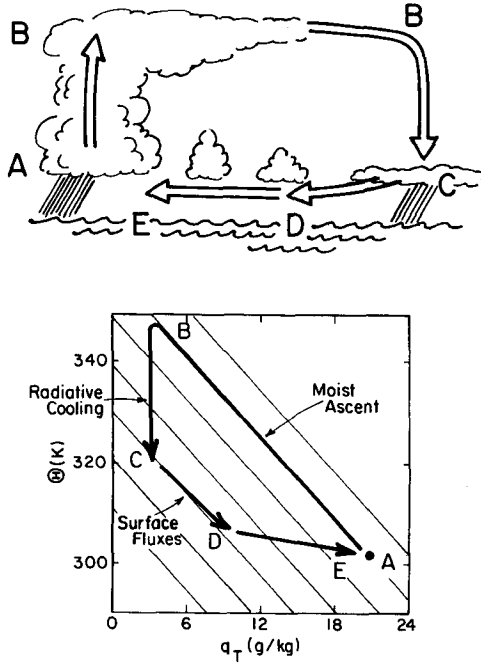


FIG. 5. A schematic of (a) the Hadley Circulation and (b) its representation on a conservative-variable diagram.

$$I(\tau = 0, \mu) = I_s \exp(-\tau^*/\mu) + \int_0^{\tau^*} B(t) \exp(-t/\mu) \frac{dt}{\mu}, \quad (1)$$

where I_s is the surface radiance, B is the Planck black-body function, and $I(\tau = 0, \mu)$ is the radiance at the satellite altitude represented here for a given view angle θ , where $\theta = \cos^{-1}\mu$. In general, channels 4 and 12 occur in that part of the spectrum where the optical depth τ^* of the atmospheric column defined from the satellite to the surface is large so that the surface term in (1) is negligibly small. Simulations are only carried out for nadir view angles (i.e., $\mu = 1$) throughout since a priori angular corrections were applied to the radiance data as described previously.

Simulation of satellite-measured radiances based on (1) requires some kind of spectral integration that includes in these integrals the instrument filter response functions. In this study we calculate the quantity

$$I(\tau = 0, \mu) = \sum_{j=1}^N f_j \Delta\nu_j \left[I_{s,j} \mathcal{T}_j(\tau_j^*, 0, \mu) + \int_0^{\tau_j^*} B_j(t_j) \mathcal{T}_j(t_j, 0, \mu) \frac{dt_j}{\mu} \right], \quad (2)$$

where the spectral integration is carried out as a summation over a finite number of N subintervals of spectral width $\Delta\nu_j$, chosen to resolve the spectral structure

of the sensor filter function f_j . The band transmission function follows as

$$\mathcal{T}_j(\tau, 0, \mu) = \frac{1}{\Delta\nu_j} \int_{\Delta\nu_j} \exp(-\tau_\nu/\mu) d\nu. \quad (3)$$

a. Band transmission

The crux of any satellite radiance simulation approach lies in the treatment of the transmission function to represent the absorption by the gas or gases in question (for this study these gases are CO_2 , H_2O , and O_3). For the j th subinterval, the transmission functions used are based on the Malkmus band model (Malkmus 1967) formula

$$\mathcal{T}_j(u) = \exp \left[-\frac{\pi\alpha_j}{2} (1 + 4S_j u / \pi\alpha_j)^{1/2} \right], \quad (4)$$

where u is the vertical pathlength of the absorbing gas, α the effective line half-width, and S the effective line strength. These band parameters α and S are related to statistical line parameters

$$S_j = \frac{1}{N_j \delta_j} \sum_i s_i$$

and

$$\alpha_j = \frac{4}{\pi S_j \delta_j} \left[\frac{1}{N_j} \sum_i (s_i \alpha_i)^{1/2} \right]^2,$$

where N_j are the number of lines in the j th spectral band of width $\Delta\nu_j$, and the mean line spacing within this band is

$$\delta_j = \Delta\nu_j / N_j.$$

Values of the band parameters S_j and α_j used in this study are discussed below. The method of using band model transmission functions is fairly standard and has been used to model the IR transfer for by Shine (1991), Slingo and Webb (1992), and Ellingson et al. (1989) and has been explored in relation to k -distribution methods by Lacis and Oinas (1991). This study employs pressure and temperature scaling techniques referred to as the van de Hulst–Curtis–Godson method (Goody and Yung 1989). Channels 4 and 6 are modeled assuming CO_2 – H_2O – O_3 overlap, which is treated through a multiplication of the transmission functions of each gas.

The channel transmission functions, defined as

$$\bar{\mathcal{T}}(\tau, 0, \mu) = \frac{\sum_{j=1}^N f_j \mathcal{T}_j(\tau, 0, \mu)}{\sum_{j=1}^N f_j}, \quad (5)$$

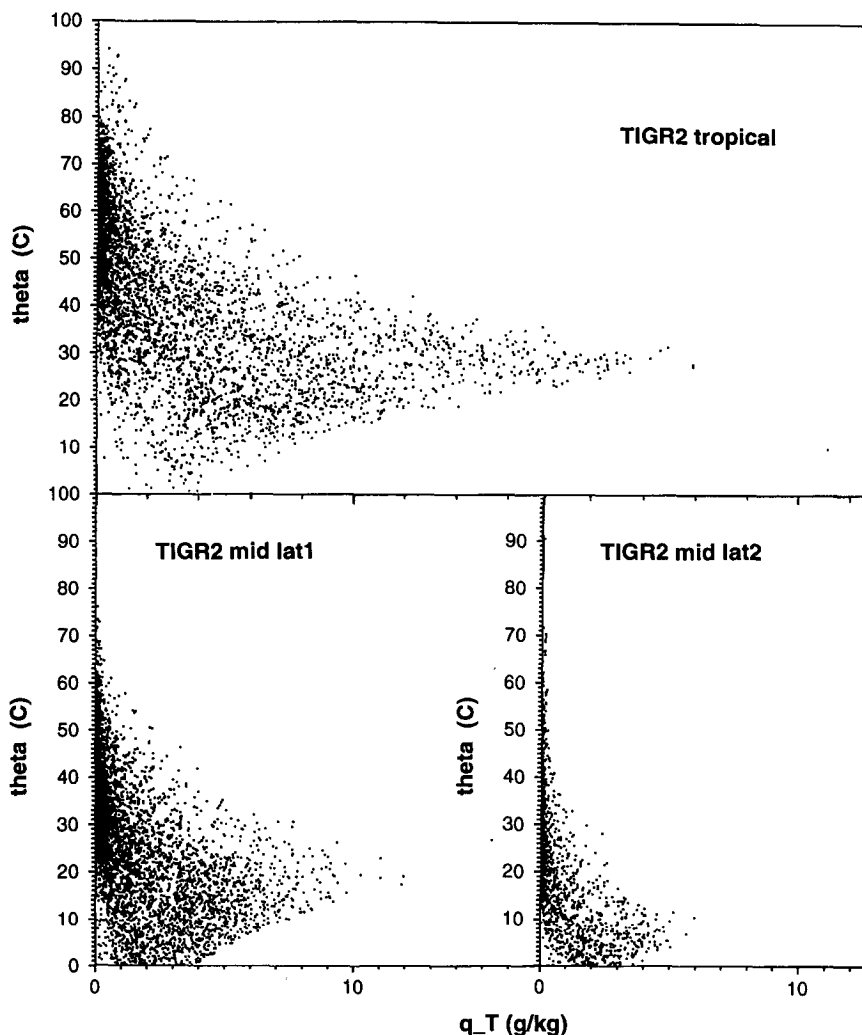


FIG. 6. The TIGR2 tropical and midlatitude profiles on θ - q_T conservative variable diagrams.

where the summation is over the band defined by the channel filter function f_j , were evaluated at a resolution of 1 cm^{-1} using MODTRAN92 (Berk et al. 1989) at fixed temperatures and pressures. Malkmus band model parameters were then derived by fitting these MODTRAN channel transmission functions. The band parameters so derived are given in Table 2 and a comparison between the band model transmission and MODTRAN-derived transmissions is shown in Fig. 7 as a function of the constant pressure absorber path length. The transmissions shown in this diagram exclude contributions by water vapor continua.

The radiative transfer model using the band transmission functions and band-corrected Planck functions specific to each channel (e.g., Weinreb et al. 1981) was used to simulate channel brightness temperatures for each of the 1761 TIGR2 atmospheric profiles. The re-

sults of these calculations are shown in Fig. 8a for channel 12 and are contrasted against the corresponding brightness temperatures derived using MODTRAN. Two sets of MODTRAN simulations are shown on the diagram. In one case, only line absorption was assumed whereas the second set of simulations include a water vapor continuum overlap (simulated continuum contributions to channels 4 and 6 were deemed to be small and were not included). From this diagram we conclude that the simple band model results for channel 12 agree well with the line absorption results of MODTRAN with an rms difference of 0.6 K. Addition of continuum absorption by foreign broadening shifts the brightness temperatures in the mean by 2 K (Fig. 8b). We account for this absorption using a transmission function of the form

$$\mathcal{T}(\tau, 0) = \exp[-t_{\text{cont}}], \quad (6)$$

where the continuum optical depth (S. A. Clough, 1994 personal communication) is

$$t_{\text{cont}} = c\nu_0 \left(\frac{p}{p_0} \right) \left(\frac{T_0}{T} \right) u.$$

Here u is the vertical path of water vapor, p and T are path pressure and temperatures, $T_0 = 273$ K and $p_0 = 1013$ hPa, c is a coefficient defining the foreign broadening continuum absorption and is obtained from Clough (1993), and ν_0 is the central wavenumber of the band. Both ν_0 and c are given in Table 2 for each channel. The transmission of channel 12 is then the product of (6) and (4). The calculated bias between MODTRAN and the model using this form of transmission is 0.5 K, and the rms difference in brightness temperature between these models is 0.6 K.

Similar brightness temperature comparisons are presented in Figs. 9a,b for channels 4 and 6, respectively. Whereas a continuum component is also included in modeling the transmission of these channels, its effect on the radiative transfer of channels 4 and 6 is small relative to its effect on channel 12. The rms differences between MODTRAN and the model brightness temperatures are 0.6 K and 1 K respectively for channels 4 and 6.

5. The physical basis for the retrieval of UTH and column overburden

a. A simple model of 6.7- μm radiative transfer

Soden and Bretherton (1993, hereafter SB) introduced a simple model of the 6.7- μm radiative transfer and subsequently used it to identify the key relationship between relative humidity and the GOES 6.7- μm brightness temperature. Here we adopt this method with some changes and use it as the framework for the present retrieval. The SB model solves the equation

$$I = \int_0^\infty e^{-t} \frac{dB}{dp} dp, \quad (7)$$

which resembles the radiative transfer equation (1) with the omission of the surface term. The essence of the model and key to the retrievals described below lies in the assumed relationships between optical depth $t(p)$ at pressure p , relative humidity r , and column vapor overburden u_* . It is relatively simple to show that line transmission at 6.7 μm closely obeys the square root dependence

$$t(p) = k[u(p)]^{1/2}, \quad (8)$$

where k is a proportionality constant (excluding any continuum effects discussed in more detail below, we determine that $k = 1.85 \text{ m kg}^{-1/2}$ for channel 12 of TOVS, similar to the value of $1.80 \text{ m kg}^{-1/2}$ given by SB for the GOES channel). The path is

$$u(p) = \frac{18}{29} \int_0^p r \frac{e_s}{p} \frac{dp}{g}, \quad (9)$$

where g is the acceleration by gravity. It is important to note that (8) excludes continuum contributions that are shown to be relevant later.

With the following approximations,

$$e_s(T) = e_s(T_0) \exp \left[\lambda \frac{T'}{T_0} \right] \quad (10)$$

for the saturation vapor pressure at a temperature $T' = T - T_0$, where T_0 is a reference temperature taken to be 240 K and $\lambda = 23.1$, and

$$p = p_0 \exp \left[\frac{T'}{\beta T_0} \right] \quad (11)$$

for pressure, where p_0 is the pressure at T_0 and β is a lapse rate factor. Substitution of (10) and (11) into (9) yields

$$u(p) = u_0 \exp[\lambda T'/T_0], \quad (12)$$

assuming β and r are independent of height, and

$$u_0 = \frac{18}{29} \frac{r e_s(T_0)}{g} \frac{1}{\lambda \beta} \quad (13)$$

is the overburden above p_0 . The optical depth corresponding to this overburden follows from (8) as

$$t_0 = k u_0^{1/2}, \quad (14)$$

and combining (8), (12), and (14),

$$t = t_0 \exp \left[\frac{1}{2} \lambda \frac{T'}{T_0} \right]. \quad (15)$$

With the further approximation

$$B_\nu(T) = B_{\nu^*}(T_0) \exp \left[\eta \frac{T'}{T_0} \right] \quad (16)$$

for the Planck function (we determine $\eta = 8.3$ for channel 12), then substitution of (16) and (15) into (7) yields

$$\frac{T_{12}}{T_0} = 1 - \frac{1}{\lambda} \log t_0^2 + \frac{1}{\eta} \log \left(\frac{2\eta}{\lambda} \right)!, \quad (17)$$

which differs from that of SB only in relatively minor ways.

b. Weighting functions

The model introduced above also offers a simple way of approximating the channel 12 weighting functions. This is relevant to the retrievals described below since these weighting functions provide the vertical definition of the retrieved properties. In the earlier work of SB, five specified weighting function profiles were

TABLE 2. Malkmus band parameters for NOAA-10 HIRS
(NOAA-11 given in brackets).

Channel	Gas	$\sum S_i$ ($\text{cm}^{-1} \text{ kg}^{-1} \text{ m}^2$)	$\sum (S_i \alpha_i)^{1/2}$ ($\text{cm}^{-1} \text{ kg}^{-1/2} \text{ m}$)	c ($\text{kg}^{-1} \text{ m}^2$) [cm]	ν_0 (cm^{-1})
4	H ₂ O	0.53	1.2		
		(0.56)	(1.15)		
	CO ₂	11.18	132.45		
		(12.12)	(178.04)		
6	H ₂ O	20.67	80.11		
		(20.92)	(80.20)		
	CO ₂	4.16	15.07		
		(4.25)	(15.90)		
12	H ₂ O	17.14	1078.50	0.0822	1489
		(16.89)	(905.49)		(1480)

selected according to the value of p^* , which is a pressure parameter defined below. Alternatively, here we use the weighting function

$$\mathcal{W}(0, p) = - \frac{d\mathcal{T}(0, u)}{d \ln p} \quad (18)$$

relevant to each profile, where $\mathcal{T}(0, u)$ is given by the Malkmus band transmission function. Both relative humidity and lapse rate parameter β implied in (17) are assumed to be independent of height. In the retrieval scheme described below, these parameters are taken to be vertically averaged quantities according to the vertical averaging operator

$$\langle \cdot \rangle = \int_{p_0}^0 \cdot \mathcal{W}(0, p') d \log p'. \quad (19)$$

Figure 10 presents examples of weighting functions for three profiles, and this highlights both how the characteristics of the weighting function vary from atmosphere to atmosphere and also how broadly this function weights the relative humidity, with the peak varying from approximately 350 hPa for the tropical profile to 550 hPa for the second of the midlatitude profiles selected in these examples.

6. Results of T12 interpreted as relative humidity

a. The retrieval of UTH

Substitution of (13) into (14) produces

$$t_0 = k \left\{ \frac{18}{29} \frac{e_s(T_0)}{g} \frac{1}{\lambda} \right\}^{1/2} \left(\frac{r}{\beta} \right)^{1/2}, \quad (20)$$

and upon substitution into (17) we obtain the logarithmic relationship

$$\log \left(\frac{\langle r \rangle}{\langle \beta \rangle} \right) = a + bT12, \quad (21)$$

where both β and the relative humidity r are interpreted as averaged according to (19) above. Soden and Bretherton derive a simpler form of (21) based on the assumption that $\langle \beta \rangle$ does not vary from one atmospheric profile to another. Figure 11 shows $\langle \beta \rangle$ obtained for each of the TIGR atmospheres presented as a function of $\Delta T = T_6 - T_4$. An attempt to accommodate this variation in the retrieval was made using the relationship

$$\langle \beta \rangle = 0.10 + 0.004\Delta T, \quad (22)$$

which is based on a fit of the data in Fig. 11.

Figure 12 is an example of results derived by the radiative transfer model applied to the TIGR atmospheres using the NOAA-10 parameters and, in a way, illustrates (21). The ordinate is the left-hand side of

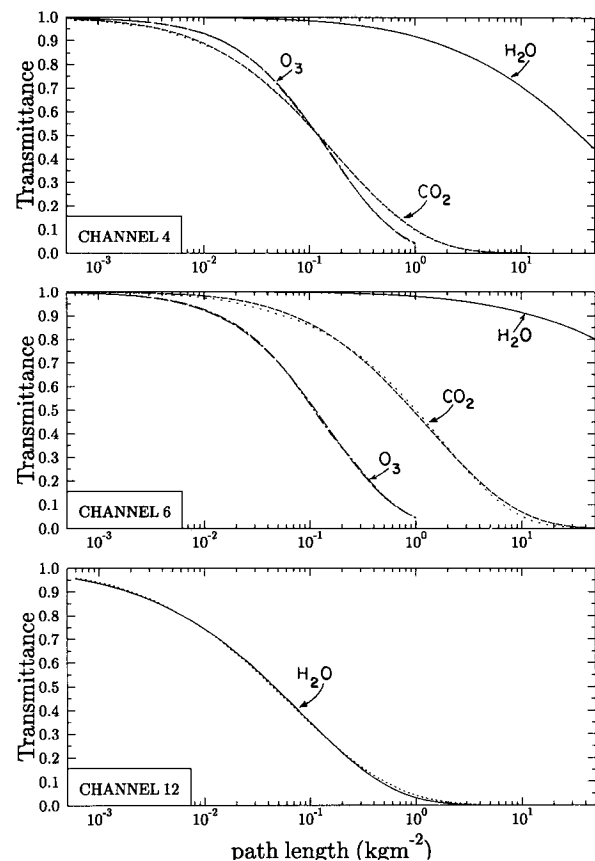


FIG. 7. Comparison between MODTRAN and Malkmus band model fits to the transmission derived using NOAA-10 filter functions. The agreement is such that the differences are generally not discernible on the diagram. The transmissions are shown as a function of the constant-pressure absorber pathlength and they exclude contributions by water vapor continua.

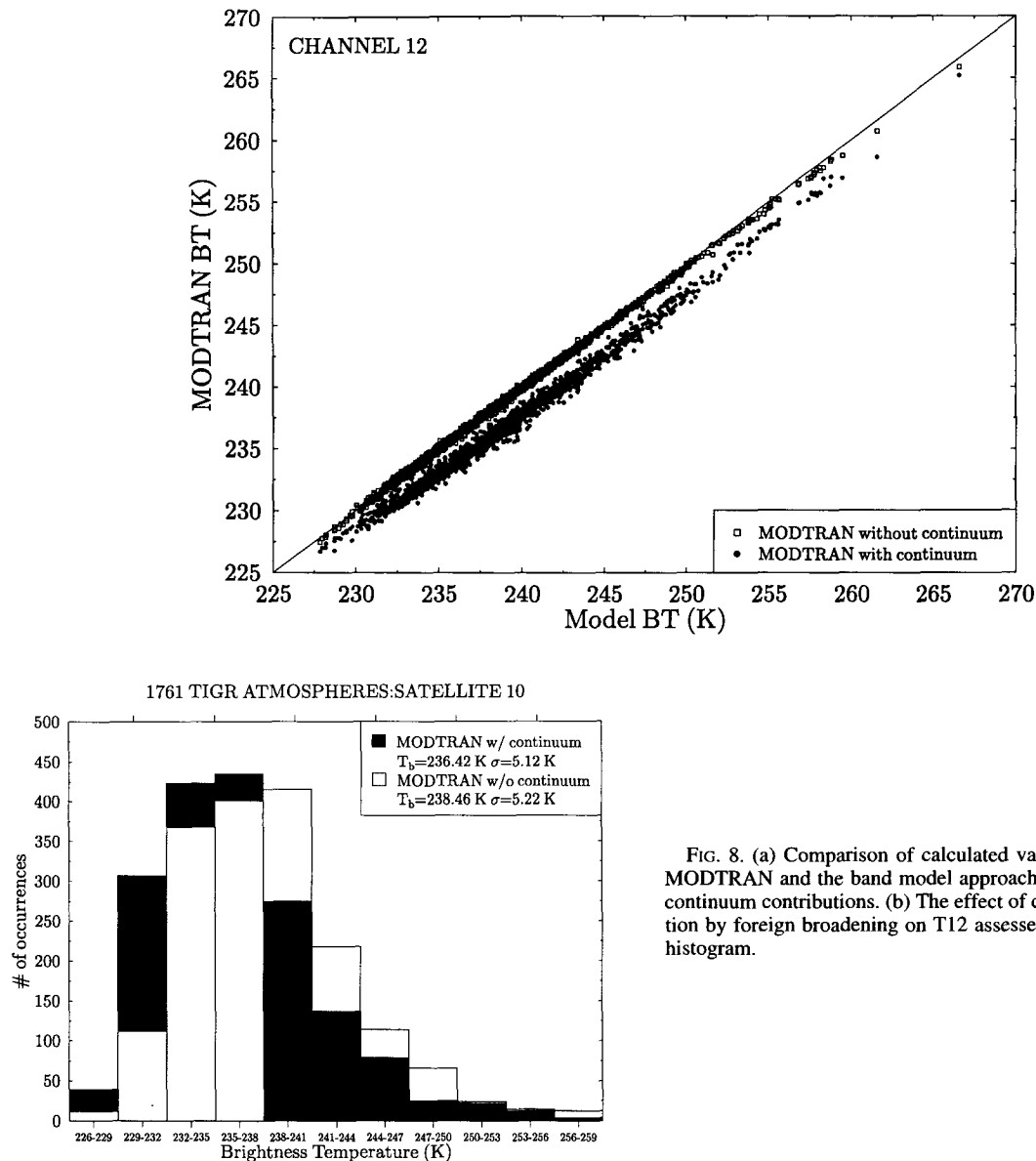


FIG. 8. (a) Comparison of calculated values of T12 using MODTRAN and the band model approach with and without continuum contributions. (b) The effect of continuum absorption by foreign broadening on T12 assessed in the form of a histogram.

(21) evaluated using derived values of $\langle r \rangle$ for each profile and $\langle \beta \rangle$ using (22) and the simulated channel 4 and 6 brightness temperatures. The abscissa is the simulated channel 12 brightness temperature, and a simple linear fit of these data provides the coefficients a and b . The original SB relationship is also presented in the diagram for comparison.

The retrieval scheme thus consists of the following steps: (i) an estimation of $\langle \beta \rangle$ using the brightness temperatures of channels 4 and 6 and (ii) an estimation of $\langle r \rangle$ from inversion of the left-hand side of (21), given the channel 12 temperatures and the coefficients derived from fits of the simulations using the *NOAA-10* and *NOAA-11* transmission model parameters.

b. Results

The pixel-level relative humidities were derived according to this procedure using pixel-level *NOAA-10* and *NOAA-11* brightness temperatures and then binned to produce daily distributions. These daily values were then averaged to produce monthly mean values of retrieved quantities, and an example is shown in Fig. 13 for January and July. Each distribution of $\langle r \rangle$ is an average of the respective months during 1989, 1990, and 1991 and clearly show the impact of large-scale circulation on the distribution of upper-tropospheric water vapor, especially equatorward of 30° latitude. For example, the prominent dry features in the subtropics are

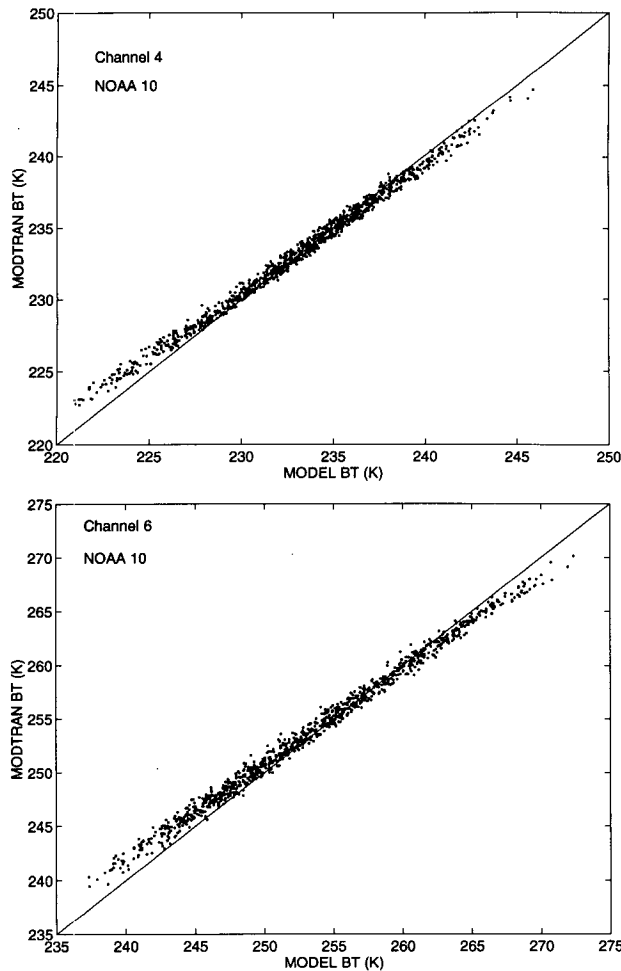


FIG. 9. Comparison of calculated values of (a) T4 and (b) T6 using MODTRAN and the band model approach.

most likely to be connected to the subsiding branch of the Hadley circulation, and the moistening in the equatorial regions is that associated with the convection in the ITCZ. The range of upper-tropospheric humidity from these dry regions varies from 10% to 30% with the moist regions exceeding 50%.

The results displayed in Fig. 13 differ from similar results reported by Soden and Bretherton (1993) using GOES data and, to a lesser extent, from the results of Schmetz and van de Berg (1994) based on Meteosat data. Values of UTH for regions of tropical convection over the Amazon reported by SB exceed the values in Fig. 13. The likely source of this difference is suggested in Fig. 14, which shows the 1989 January mean values of the retrieved UTH derived according to the scheme outlined above, where the results for each $2.5^\circ \times 2.5^\circ$ bin is plotted along the abscissa. The results are obtained using coefficients derived from simulations that exclude the effects of continuum absorption in the 6.7-

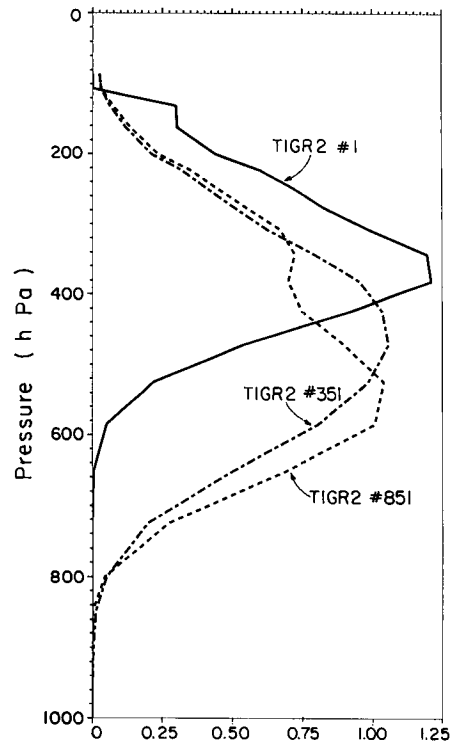


FIG. 10. Weighting functions defined according to (19) for three TIGR2 profiles (profiles 1, 351, and 851).

μm band plotted along the ordinate. The inclusion of a continuum enhances the absorption at $6.7 \mu\text{m}$ (relative to the case without this absorption), which then reduces the brightness temperature by approximately 2 K (Fig. 8b) leading to a reduction of $\langle r \rangle$ by about 15%–20%. Since uncertainties in T12 are also approximately 2 K, this difference provides a rough indication of the level of uncertainty in $\langle r \rangle$.

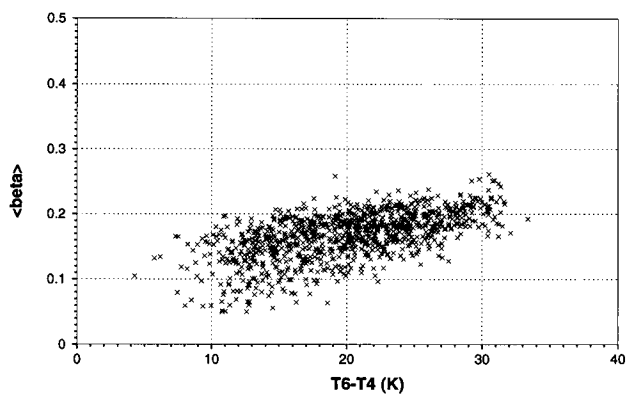


FIG. 11. The vertically weighted averaged lapse rate parameter $\langle \beta \rangle$ as a function of T4–T6.

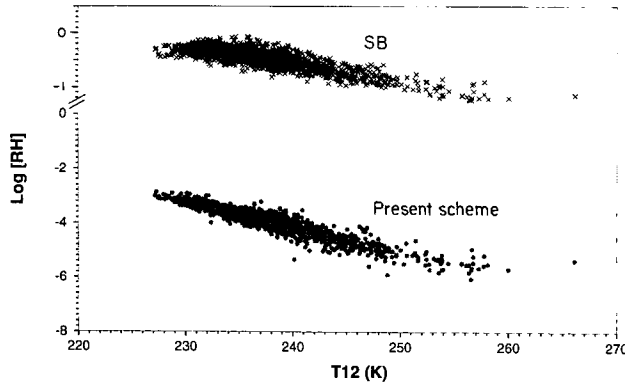


FIG. 12. The logarithm of relative humidity as a function of T12 according to simulations described in the text (referred to as present scheme) and to those of SB.

The relative humidities averaged between 30°N and 30°S and between 60°N and 60°S are shown in Fig. 15 as a function of day count. The results for the region between 0°–30°N and 0°–30°S reveal a marked annual cycle in the relative humidity with a distinct moistening occurring in the NH during the JJA season and an enhanced drying of the SH during the same season. Drying of the NH in the reciprocal season is not as large as in the SH. The 0°–60°N and S relative humidity averages possess small seasonal variations.

7. An interpretation of T12 as vapor overburden

a. The retrieval approach

An alternative way to interpret the T12 information is in terms of water vapor column overburden. The general idea is that the brightness temperature T12, when matched to the corresponding temperature profile $T(p)$ such that $T12 = T(p_*)$, defines the pressure p_* above which a constant amount of water vapor exists. This is not a new interpretation and has been explored in relation to microwave moisture sounding (e.g., Rosenkranz 1984). We explore this concept using (15) in the form

$$t_* = t_0 \exp \left[\frac{1}{2} \lambda \left(\frac{T12}{T_0} - 1 \right) \right], \quad (23)$$

where t_* is the optical depth of the column above the pressure level p_* . Rearrangement of this expression yields

$$\left(\frac{T12}{T_0} - 1 \right) = \frac{2}{\lambda} \log \left(\frac{t_*}{t_0} \right)$$

and may be equated with (17) to obtain

$$\log t_* = \frac{\lambda}{2\eta} \ln \left(\frac{2\eta}{\lambda_*} \right)! \quad (24)$$

For the values $\lambda = 22.1$ and $\eta = 8.3$, we obtain $t_* = 0.88$, and from the relationship (24), $u_* = 0.22$ mm for the column overburden above the pressure p_* . Figure 16 is the frequency distribution of u_* derived from radiative transfer computations on the TIGR2 database. The value of u_* deduced from these simulations is 0.17 mm with an rms of 0.05 mm. This is smaller than the value derived above based on the simple model since the simulations include continuum absorption and the simple model does not. We hereafter interpret the p_* pressure distribution as the 0.17 ± 0.05 mm overburden surface, and the standard deviation provides an estimate of the uncertainty of this overburden value.

Zonally averaged profiles of p_* are presented in Fig. 17 for both January and July 1989. Since the constant u_* surface generally lies above 400 hPa between 30°N and 30°S, we take the 350-hPa level to be representative of the pressure across this region and derive the overburden at this pressure in the following way. Using the retrieved values of $\langle r \rangle$ together with the value of p_* , the 350-hPa overburden is determined according to the formula

$$u_{350} = u_* + \frac{18}{29} \frac{\langle r \rangle}{g} \int_{350}^{p_*} \frac{e_s}{p} dp,$$

where the integral term represents the component added or subtracted from u_* due to the column of atmosphere either below or above p_* and the 350-hPa level. This term is evaluated using the TOVS-derived temperature profile to estimate e_s .

The average of the January and July 1989–1991 distributions of u_{350} are presented in Fig. 18. The overburden varies from 0.4 to 0.5 mm in regions associated with deep convection in the Tropics to values in the range below 0.1 mm in drier regions of subsidence in the subtropics and for air generally poleward of 30° latitude. In Fig. 19 u_{350} averaged between 30°N and 30°S is shown as a function of day count in a manner analogous to Fig. 15a. The annual cycle of the 0°–30°N and 0°–30°S averaged overburden reveals a seasonal character similar to that of relative humidity shown previously in Fig. 15.

The extent to which the differences in overburden between each hemisphere, particularly in the respective wintertime seasons, is a result of wintertime differences in large-scale circulation in each hemisphere needs to be explored. To emphasize these hemispheric differences, Hovmöller analyses of pentad u_{350} are presented in Figs. 20a–c for overburden averaged over the three latitude strips from 5°N to 5°S (Fig. 20a), 22.5°N to 27.5°N (Fig. 20b), and 22.5°S to 27.5°S (Fig. 20c). Time runs down the page beginning on 1 January 1989 at the upper edge of each diagram and ending on 31 December 1991 at the bottom edge of each figure. The abscissa is longitude ranging from 0° to 360°, with the date line running through the center of each diagram.

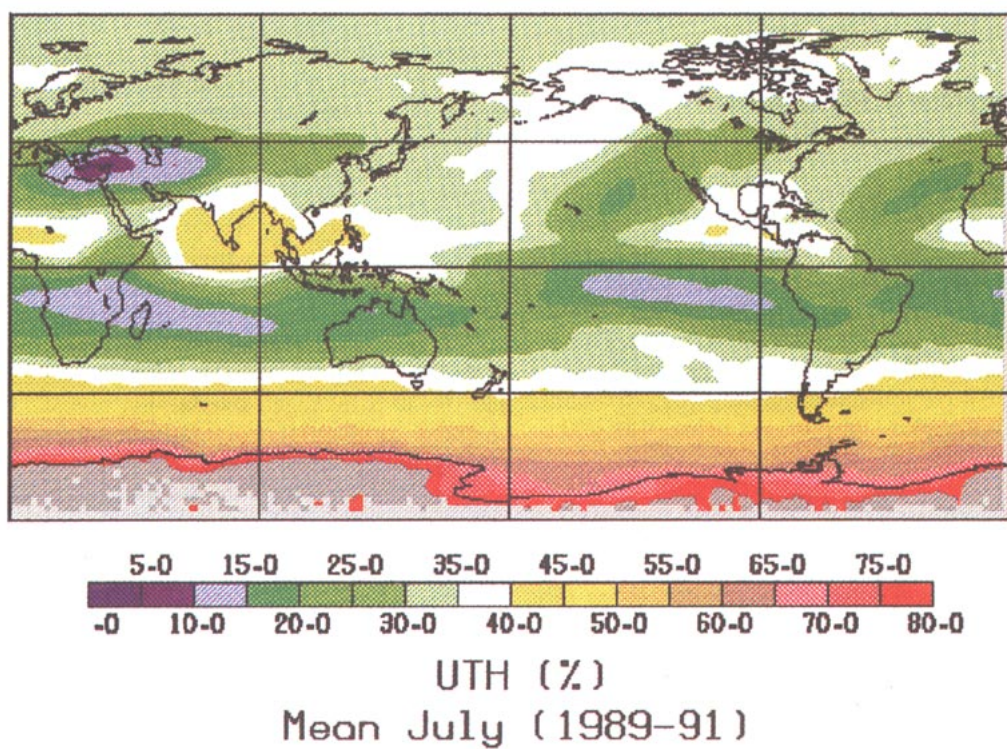
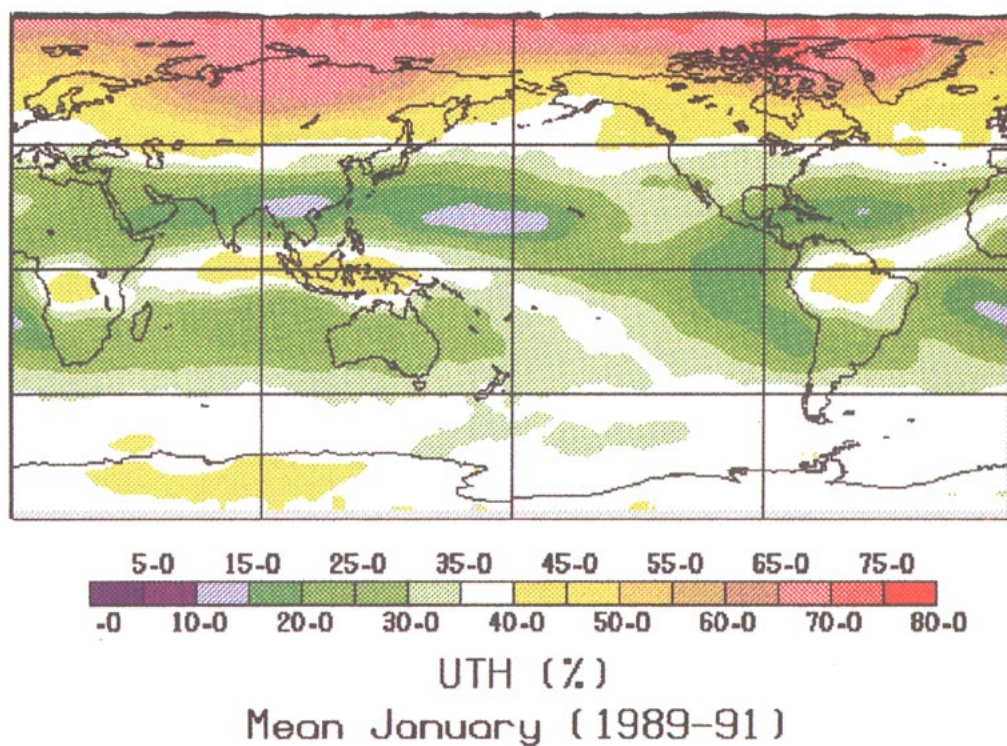


FIG. 13. A 3-year (1989-91) mean of January (upper) and July (lower) UTH.

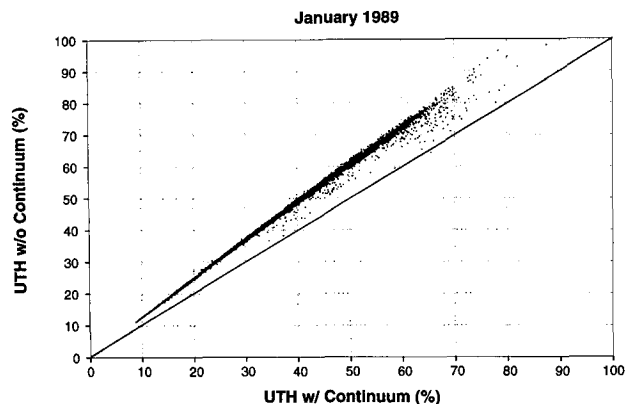


FIG. 14. The 1989 January mean values of the retrieved UTH derived according to the scheme outlined in the text. The abscissa corresponds to results obtained using coefficients derived from simulations that include the effects of continuum absorption in the $6.7\text{-}\mu\text{m}$ band, and the ordinate refers to retrievals based on exclusion of continuum absorption.

These diagrams reveal a number of remarkable features of upper-tropospheric water vapor in the region defined by the Hadley circulation. In the equatorial region, east

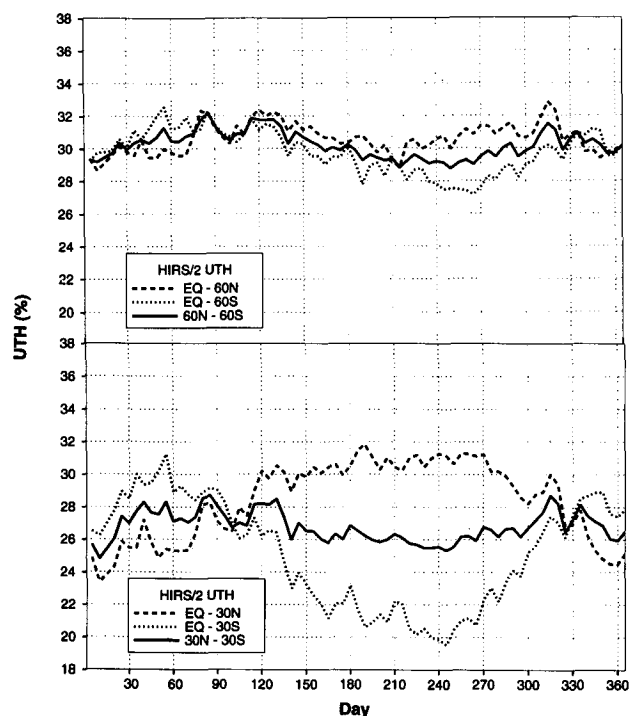


FIG. 15. The relative humidities averaged between 30°N and 30°S (lower) and between 60°N and 60°S (upper) as a function of day count.

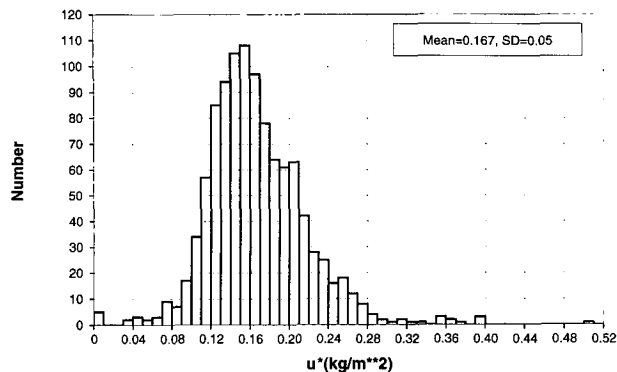


FIG. 16. The water vapor overburden above p_* derived from simulated values of T12 and matched to the corresponding TIGR2 profile.

— west differences in upper-tropospheric water vapor are large. Relatively moist air (in excess of 0.4 mm) is located in western regions of the equatorial Pacific in regions of prominent ascent associated with deep convection, and dry air (with values below 0.1 mm) occurs in the eastern Pacific. This is consistent with the conventional notion of the Walker circulation, with ascent to the west and descent over the eastern Pacific. The quantitative link between the Walker circulation and these west–east gradients in upper-tropospheric moisture needs to be addressed in future studies.

The averaged values of u_{350} between 22.5° and 27.5° latitude are used to examine water vapor features in areas associated with the subsidence branch of the wintertime Hadley circulation. Hovmöller diagrams of these averaged data point to the reasons for the hemispheric asymmetries in both relative humidity and overburden noted in the discussion of results presented in previous diagrams. The NH upper troposphere at

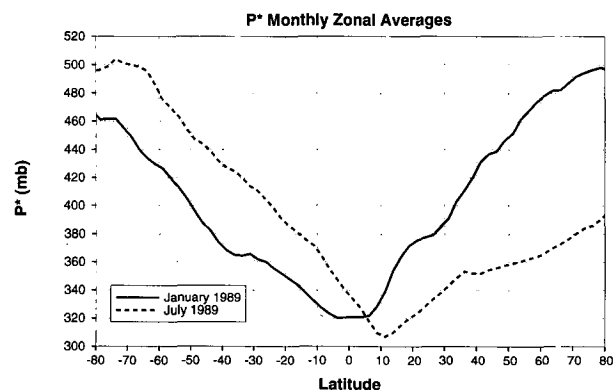


FIG. 17. January 1989 and July 1989 zonal-averaged profiles of p_* .

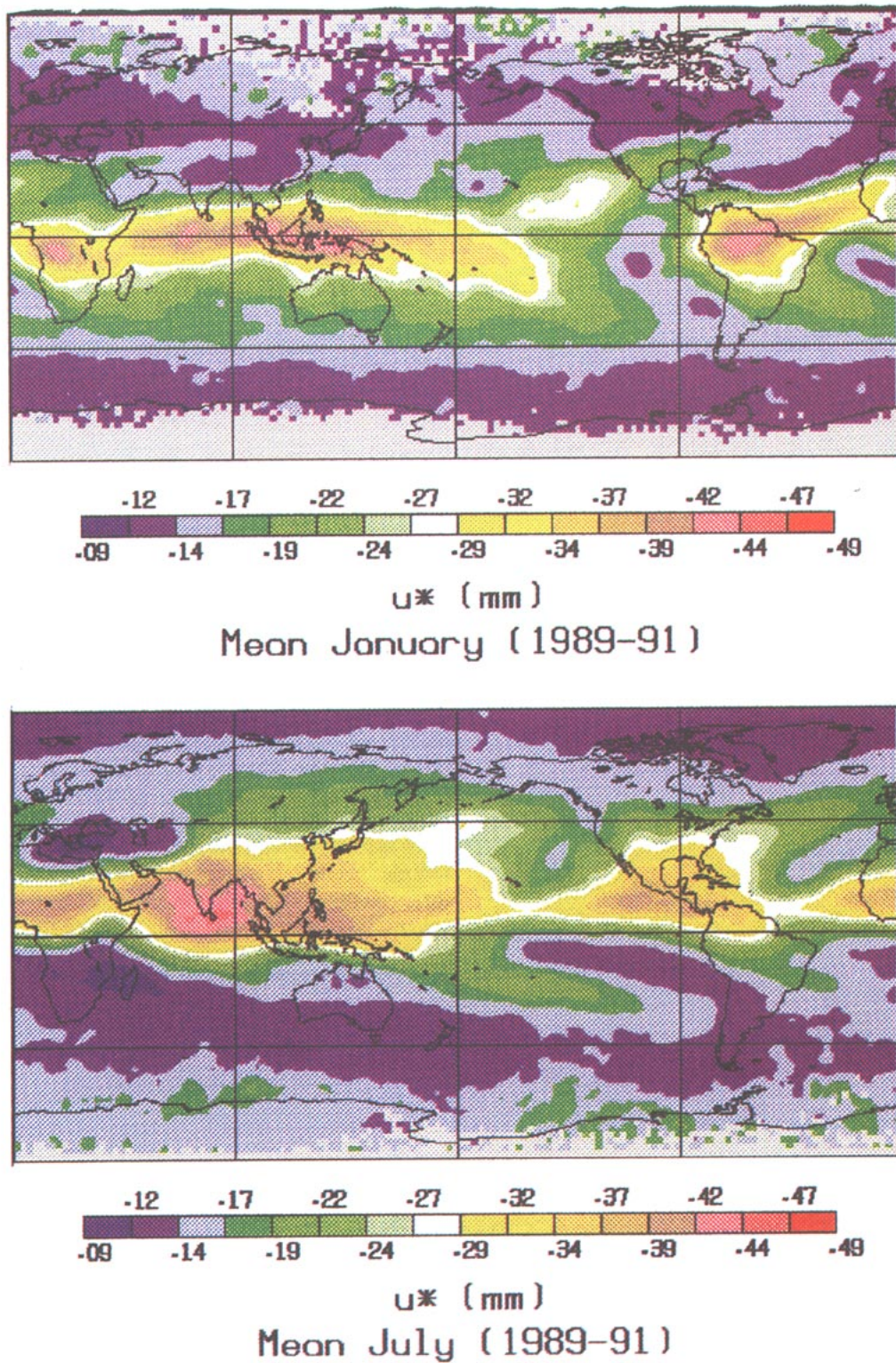


FIG. 18. A three-year (1989-91) mean of January (upper) and July (lower) overburden u_{350} .

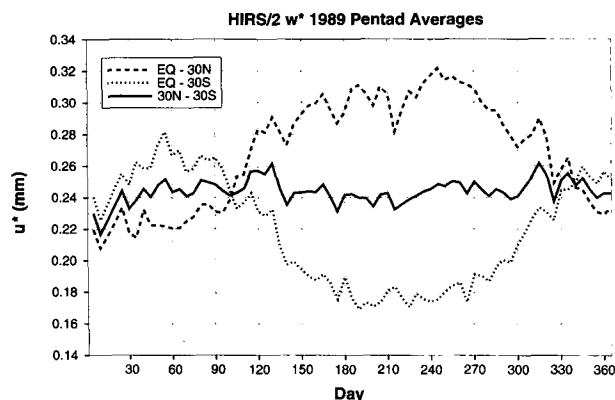


FIG. 19. The pentad u_{350} averaged between 30°N and 30°S as a function of the 1989 day count.

these latitudes is moistened significantly by the effects of monsoonal circulations identified as regions of enhanced water vapor in the region between 60°E and the date line and in the region of the Northern American monsoon centered over 90°W. Moistening by the Southern Hemisphere monsoon is much less distinct, but the wintertime drying between 0° and 180°E is greatly enhanced. Dry upper-tropospheric air persists throughout the year in the region over the southern Pacific centered at approximately 90°W. This region is one of prevalent low cloudiness.

The lack of penetration of moist air into the Southern Hemisphere subtropics is more clearly illustrated in the latitude–time plots shown in Fig. 21. Here u_{350} is shown for latitudes from 35°S to 35°N along the longitudes 90°E, 180°, and 90°W for the three-year period from January 1989 to December 1991. A feature of the time series at 90°E is the lack of symmetry in the poleward extents of moist upper-tropospheric air (taken here to be $u_{350} > 0.25$ mm) in each hemisphere. Moist air protrudes to 35°N during the Northern Hemisphere summer, whereas the Southern Hemisphere extent of this air is limited to about 10°S with little seasonality. The variation of moist upper-tropospheric air over the date line exhibits a more regular seasonal migration from the SH in summer to the Northern Hemisphere and back. The characteristics of moisture over 90°W fall between the two regimes that seem to characterize the variations over 90°E and 180°. At 90°W, the moistening of upper-tropospheric air in the NH from spring to fall is punctuated during winter by excursions of Southern Hemispheric air that remains dry throughout the year.

8. Summary and conclusions

This paper describes a physically based method for the retrieval of upper-tropospheric humidity and upper-tropospheric column water vapor based on the use of

radiance data collected by TOVS, principally channels 4 (14.2 μm), 6 (13.7 μm), and 12 (6.7 μm). This research expands on similar research based on the 6.7- μm channel radiance measurements on geostationary satellites (Schmetz and van de Berg 1994; Soden and Bretherton 1993) and research based on the use of similar data available from polar orbiting satellites.

From analyses of the data obtained with the retrieval, we conclude that:

(i) TOVS radiance data, particularly that of the upper-tropospheric water vapor channel 12, can be modeled usefully using a single band Malkmus model with parameters tuned to a particular sensor on a particular satellite. A significant uncertainty exists due to continuum absorption, even in regions where line absorption is dominant. This uncertainty could introduce a bias as large as 2 K that in turn leads to an uncertainty of approximately 15%–20% in the retrieved UTH and UTCWV. High-precision, high-spectral-resolution measurements of the emission spectra are critically important for shedding further light on the complex issue of continuum absorption in the spectral region defined by TOVS channel 12.

(ii) In addition to these emission measurements, there is also a critical need for high-accuracy measurements of upper-tropospheric water vapor to test retrievals such as the one described in this paper. Despite the broad lack of data suitable for global validation purposes, the fundamental importance of water vapor to climate, and especially water in the upper troposphere, dictates that these satellite data be analyzed if for no other reason than to provide motivation for further validation efforts.

(iii) The results presented in this paper suggest that the relative humidity of the upper troposphere, especially over the domain of the Hadley circulation taken to be between 30°N and 30°S, undergoes significant seasonal variations. This is contrary to the usual assumption of fixed relative humidity adopted in simple climate feedback studies. Large seasonal changes in the region from 30°N to 30°S are associated with the seasonal swings in the Hadley circulation. Similar seasonal changes in the 350-hPa overburden indicate that these swings in relative humidity occur as a result of significant seasonal shifts in the upper-tropospheric water vapor content.

(iv) In the region equatorward of 30° latitude, the Southern Hemisphere winter is significantly drier than the Northern Hemisphere winter, which is also consistent with the findings of Kelly et al. (1991) based on analyses of aircraft data, although in regions poleward of 30° latitude. This drying is associated with expansive regions of subsidence producing dry upper-tropospheric air across most of the SH. A more quantitative association between these observations and general circulation will be the topic of a future study, but these

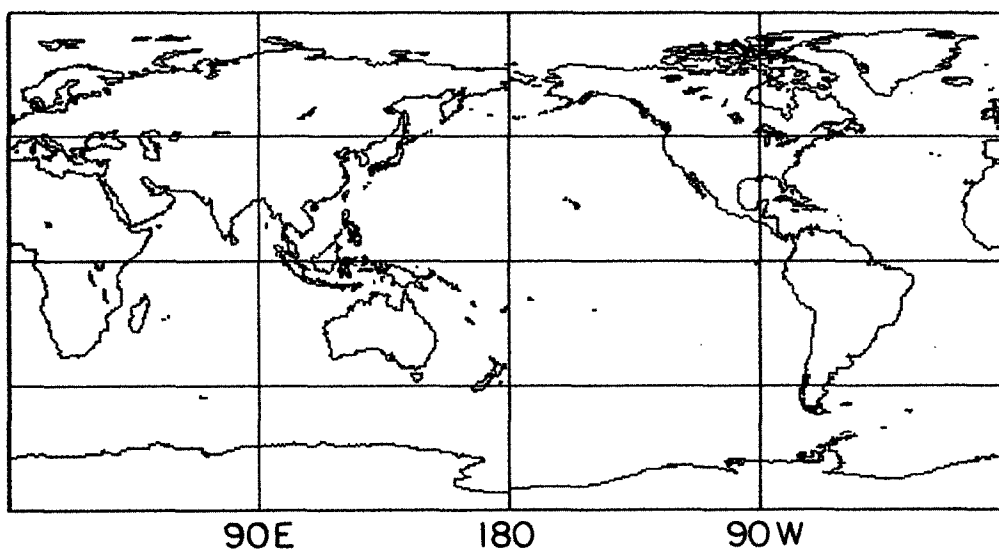
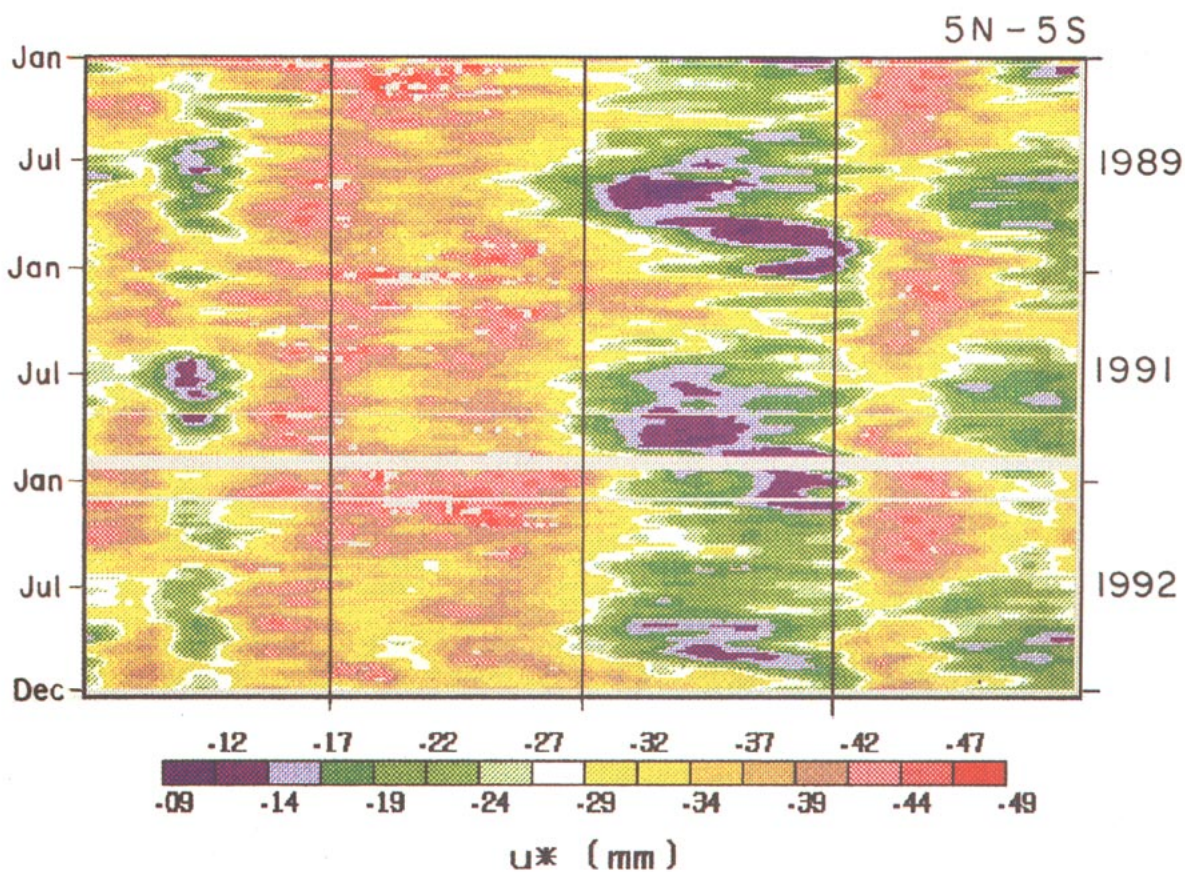


FIG. 20. Hovmöller analyses of pentad u_{350} averaged over the three latitude strips from (a) 5°N to 5°S, (b) 22.5°N to 27.5°S, and (c) 22.5°S to 27.5°S. Time runs down the page beginning on 1 January 1989 at the upper edge of each diagram and ending on 31 December 1991 at the bottom edge of each figure. The abscissa is longitude stretching from 0° to 360°, with the date line running through the center of each diagram.

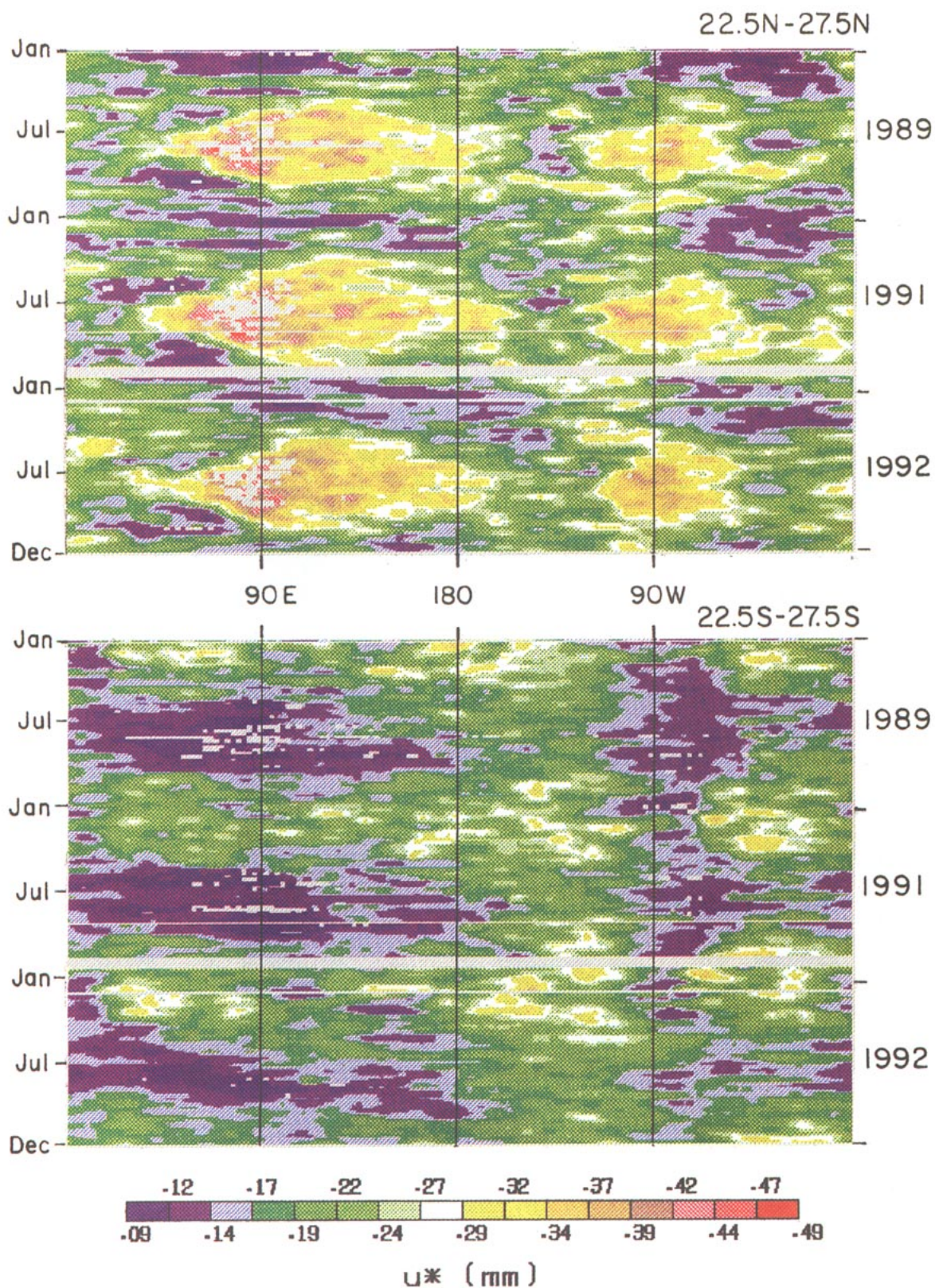


FIG. 20. (Continued)

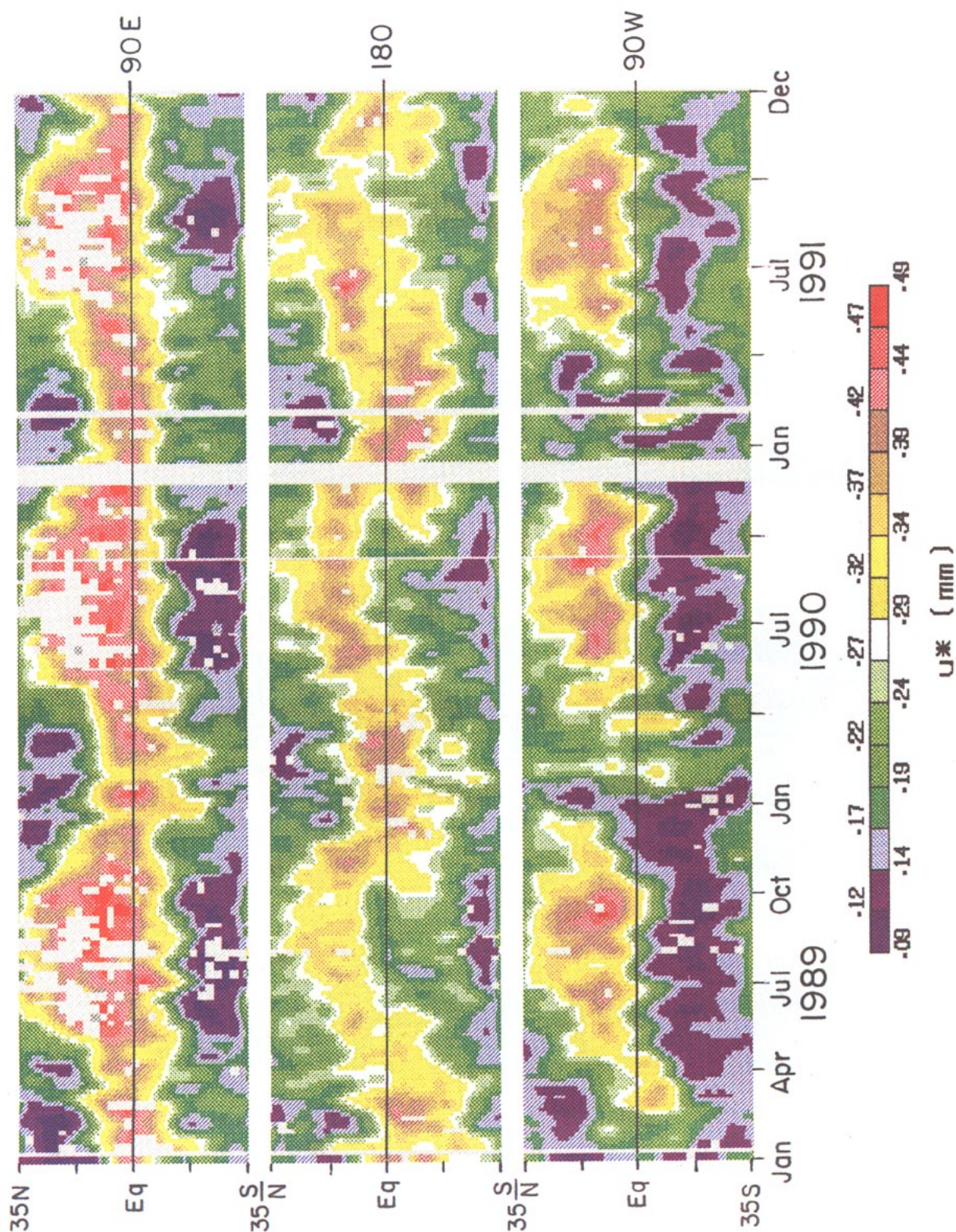


FIG. 21. Latitude-time plots of pentad μ_{50} shown for latitudes from 35°S to 35°N at fixed longitudes of 90°E, 180°E, and 90°W for the 3-year period from January 1989 to December 1991.

results are suggestive of a difference in the large-scale circulations of each hemisphere. As an example, analyses of the data show the clear effects of moistening in the NH subtropics through the monsoonal circulations over Asia and North America and the lack of penetration of the SH monsoon in the Southern Hemisphere subtropics, thus implying that differences in landmass distributions govern the way water vapor is processed between the Tropics and midlatitudes.

It is implied in the results described in this paper that global information on upper-tropospheric moisture is a surrogate for global information on vertical motions in the upper troposphere and cloudiness. The extent to which the water vapor overburden results discussed in this paper correlate to dynamics, cloudiness, and precipitation is an important topic and one that will be pursued in a related study.

Acknowledgments. This work was supported by NOAA Contract NA3RJ0202-ITEM 2. Discussion with Brian Soden and John Bates at various stages of this research was valuable.

REFERENCES

- Bates, J. J., X. Wu, and D. L. Jackson, 1996: Interannual variability of upper troposphere water vapor band brightness temperature. *J. Climate*, **9**, 427–438.
- Berk, A., L. S. Bernstein, and D. C. Robertson, 1989: MODTRAN: A moderate resolution model for LOWTRAN 7. GL-TR-89-0122, 38 pp. [Available from Spectral Sciences, Inc., 99 South Bedford St., 7, Burlington, MA 01803].
- Betts, A. K., 1990: Greenhouse warming and the tropical water vapor budget. *Bull. Amer. Meteor. Soc.*, **71**, 1465–1467.
- Boers, R., and A. J. Prata, 1995: Thermodynamic structure of the maritime troposphere around the Australian continent. *Int. J. Climate*, submitted.
- Bony, S., and J. P. Duvel, 1994: Influence of the vertical structure of the atmosphere on the seasonal variation of precipitable water and greenhouse effect. *J. Geophys. Res.*, **99**(12), 12 963–12 980.
- Clough, S. A., 1993: Radiative transfer model development in support of the atmospheric radiation measurement program. *Proc. Third ARM Science Team Meeting*, Dept. of Energy, Norman, OK, 11–17.
- Ellingson, R. G., D. J. Yanuk, H.-T. Lee, and A. Gruber, 1989: A technique for estimating outgoing longwave radiation from HIRS radiance observations. *J. Atmos. Oceanic Technol.*, **6**, 706–711.
- Elliott, W. P., and D. J. Gaffen, 1991: On the utility of radiosonde humidity archives for climate studies. *Bull. Amer. Meteor. Soc.*, **72**, 1507–1520.
- Goody, R. M., and Y. L. Yung, 1989: *Atmospheric Radiation: Theoretical Basis*. Oxford University Press, 519 pp.
- Hayden, C. M., W. L. Smith, and H. M. Woolf, 1981: Determination of moisture from NOAA polar orbiting satellite sounding radiances. *J. Appl. Meteor.*, **20**, 450–466.
- Kelly, K. K., A. F. Tuck, and T. Davies, 1991: Wintertime asymmetry of upper tropospheric water between the Northern and Southern Hemispheres. *Nature*, **353**, 244–247.
- Kidwell, K. B., 1991: *NOAA Polar Orbiter Data User's Guide*. NOAA/National Environmental Satellite, Data, and Information Service, Washington, D.C., 312 pp.
- Lacis, A. A., and V. Oinas, 1991: A description of the correlated k distribution method for modeling nongray gaseous absorption, thermal emission, and multiple scattering in vertically inhomogeneous atmospheres. *J. Geophys. Res.*, **96**, 9027–9063.
- Lindzen, R. S., 1990: Some coolness concerning global warming. *Bull. Amer. Meteor. Soc.*, **71**, 288–299.
- Malkmus, W., 1967: Random Lorentz model with exponential-tailed s^{-1} line intensity distribution function. *J. Opt. Soc. Amer.*, **57**, 323–329.
- McMillin, L. M., and C. Dean, 1982: Evolution of a new operational technique for producing clear radiances. *J. Appl. Meteor.*, **20**, 1005–1014.
- Peixoto, J. P., and A. H. Oort, 1992: *Physics of Climate*. American Institute of Physics, 520 pp.
- Pierrehumbert, R. T., 1994: Thermostats, radiator fins and local runaway greenhouse. *J. Atmos. Sci.*, **52**, 1784–1806.
- , and H. Yung, 1993: Global chaotic mixing on isentropic surfaces. *J. Atmos. Sci.*, **50**, 2462–2480.
- Raschke, E., and W. R. Bandeen, 1967: A quasi-global analysis of tropospheric water vapor content and its temporal variations from radiation data of the meteorological satellite TIROS IV. *Space Res.*, **VII**, 920–931.
- Rind, D., E. W. Chiou, W. Chu, J. Larsen, S. Oltmans, J. Lerner, M. P. McCormick, and L. McMaster, 1991: Positive water vapor feedback in climate models confirmed by satellite data. *Nature*, **349**, 500–503.
- Rosenkranz, P. W., M. J. Komichak, and D. H. Staelin, 1982: A method for estimation of atmospheric water vapor profiles by microwave radiometry. *J. Appl. Meteor.*, **21**, 1364–1370.
- Schmetz, J., and L. van de Berg, 1994: Upper tropospheric humidity observations from Meteosat compared with short-term forecast fields. *Geophys. Res. Lett.*, **21**, 573–578.
- Scott, N. A., A. Chedin, V. Achard, B. Bonnet, F. Cheruy, C. Claud, J. Escobar, N. Husson, H. Rieuu, Y. Tahani, and B. Tournier, 1991: Recent advances in the 3D thermodynamic analysis of the Earth system through the “3I” algorithm: Extension to the second generation vertical sounders. Internal Publication Atmospheric Radiation Analysis Group, LMD CNRS France, 50 pp.
- Shine, K. P., 1991: On the cause of the relative greenhouse strength of gases such as Halocarbons. *J. Atmos. Sci.*, **48**, 1513–1518.
- Slingo, A., and M. J. Webb, 1992: Simulation of clear-sky outgoing longwave radiation over the oceans using operational analyses. *Quart. J. Roy. Meteor. Soc.*, **118**, 1117–1144.
- Smith, W. L., H. M. Woolf, C. M. Hayden, D. Q. Wark, and L. M. McMillin, 1979: The TIROS-N operational vertical sounder. *Bull. Amer. Meteor. Soc.*, **58**, 1177–1187.
- Soden, B. J., and F. P. Bretherton, 1993: Upper tropospheric relative humidity from the GOES 6.7 μm channel: Method and climatology for July 1987. *J. Geophys. Res.*, **98**, 16 669–16 688.
- Stephens, G. L., 1990: On the relationship between water vapor over the oceans and sea surface temperature. *J. Climate*, **3**, 634–645.
- , and T. J. Greenwald, 1991: The earth's radiation budget and its relation to atmospheric hydrology. Part I: Observations of the clear sky greenhouse effect. *J. Geophys. Res.*, **96**, 15 311–15 324.
- , A. Slingo, M. J. Webb, P. J. Minnett, P. H. Daum, L. Klienman, I. Wittmeyer, and D. A. Randall, 1994: Observations of the earth's radiation budget in relation to atmospheric hydrology. Part IV: Atmospheric column radiative cooling over the World's Oceans. *J. Geophys. Res.*, **99**, 18 585–18 604.
- Swaroop, A. A., J. Nappi, H. J. Bloom, and L. M. McMillan, 1988: A method of noise reduction for the improvement of clear column radiance estimation in partly cloudy areas. *Proc. Third Conf. Satellite Meteorology and Oceanography*, Anaheim, CA, Amer. Meteor. Soc., 13–15.

- van de Berg, L., A. Pyomjamsri, and J. Schmetz, 1991: Monthly mean upper tropospheric humidities in cloud-free areas from meteosat observations. *Int. J. Climatol.*, **11**, 819–828.
- Webb, M. J., A. Slingo, and G. L. Stephens, 1994: Seasonal variations of the clear-sky greenhouse effect: The role of changes in atmospheric temperatures and humidities. *Climate Dyn.*, **9**, 117–129.
- Weinreb, M. P., H. E. Fleming, L. M. McMillin, and A. C. Neuen-dorffer, 1981: Transmittances for the TIROS Operational Ver-tical Sounder, NOAA Tech. Rep. NESS 85, U.S. Dept. of Com-merce, Washington, D.C., 60 pp.
- Werbowetzki, A., 1981: Atmospheric sounding user's guide. NOAA Tech. Report NESS 83, U.S. Dept. of Commerce, Washington, D.C., 60 pp.
- Wu, X., J. J. Bates, and S. J. S. Khalsa, 1993: A climatology of the water vapor band brightness temperature from NOAA operational satellites. *J. Climate*, **6**, 1282–1300.